INTERFACE

royalsocietypublishing.org/journal/rsif

Research

Cite this article: Kern C, Quade M, Ray S, Thomas J, Schumacher M, Gemming T, Gelinsky M, Alt V, Rohnke M. 2019 Investigation of strontium transport and strontium quantification in cortical rat bone by time-of-flight secondary ion mass spectrometry. *J. R. Soc. Interface* **16**: 20180638. http://dx.doi.org/10.1098/rsif.2018.0638

Received: 21 August 2018
Accepted: 16 January 2019

Subject Category:
Life Sciences–Chemistry interface

Subject Areas:
biomaterials, biophysics, chemical biology

Keywords:
strontium, osteoporosis, diffusion, time-of-flight secondary ion mass spectrometry, bone nanostructure, quantification

Author for correspondence:
Marcus Rohnke
e-mail: marcus.rohnke@phys.chemie.uni-giessen.de

Electronic supplementary material is available online at http://dx.doi.org/10.6084/m9.figshare.c.4375652.

THE ROYAL SOCIETY PUBLISHING

Investigation of strontium transport and strontium quantification in cortical rat bone by time-of-flight secondary ion mass spectrometry

Christine Kern[1], Mandy Quade[2], Seemun Ray[3], Jürgen Thomas[4], Matthias Schumacher[2], Thomas Gemming[4], Michael Gelinsky[2], Volker Alt[3] and Marcus Rohnke[1]

[1]Institute of Physical Chemistry, Justus-Liebig-University Giessen, Heinrich-Buff-Ring 17, 35392 Giessen, Germany
[2]Centre for Translational Bone, Joint and Soft Tissue Research, Medical Faculty and University Hospital, Technische Universität Dresden, Fetscherstrasse 74, 01307 Dresden, Germany
[3]Experimental Trauma Surgery, Justus-Liebig University Giessen, Aulweg 128, 35392 Giessen, Germany
[4]IFW Dresden, Institute for Complex Materials, Helmholtzstrasse 20, 01069 Dresden, Germany

CK, 0000-0003-4480-4003; MS, 0000-0001-7207-7355; TG, 0000-0002-7353-595X; MR, 0000-0002-8867-950X

Next-generation bone implants will be functionalized with drugs for stimulating bone growth. Modelling of drug release by such functionalized biomaterials and drug dispersion into bone can be used as predicting tool for biomaterials testing in future. Therefore, the determination of experimental parameters to describe and simulate drug release in bone is essential. Here, we focus on Sr^{2+} transport and quantification in cortical rat bone. Sr^{2+} dose-dependently stimulates bone-building osteoblasts and inhibits bone-resorbing osteoclasts. It should be preferentially applied in the case of bone fracture in the context of osteoporotic bone status. Transport properties of cortical rat bone were investigated by dipping experiments of bone sections in aqueous Sr^{2+} solution followed by time-of-flight secondary ion mass spectrometry (ToF-SIMS) depth profiling. Data evaluation was carried out by fitting a suitable mathematical diffusion equation to the experimental data. An average diffusion coefficient of $D = (1.68 \pm 0.57) \cdot 10^{-13}$ cm^2 s^{-1} for healthy cortical bone was obtained. This value differed only slightly from the value of $D = (4.30 \pm 1.43) \cdot 10^{-13}$ cm^2 s^{-1} for osteoporotic cortical bone. Transmission electron microscopy investigations revealed a comparable nano- and ultrastructure for both types of bone status. Additionally, Sr^{2+}-enriched mineralized collagen standards were prepared for ToF-SIMS quantification of Sr^{2+} content. The obtained calibration curve was used for Sr^{2+} quantification in cortical and trabecular bone in real bone sections. The results allow important insights regarding the Sr^{2+} transport properties in healthy and osteoporotic bone and can ultimately be used to perform a simulation of drug release and mobility in bone.

1. Introduction

Osteoporosis is a systemic bone disease, characterized by a reduction in bone density [1]. In recent years, there was a growing interest in strontium as an orally administered therapeutic agent in osteoporosis therapy due to the dual effect of Sr^{2+} ions on bone metabolism: they promote new bone formation by stimulating osteoblasts and simultaneously inhibit osteoclastic bone resorption. These beneficial effects lead to accelerated bone growth, which was shown in numerous studies [2–5].

Additionally, it was shown that treatment with strontium ranelate improves implant osseointegration [3,6,7]. However, the bioavailability of

pharmaceutically active Sr^{2+} ions by oral medication is only about 20% [8] and systemic treatment of osteoporosis with strontium ranelate is associated with some adverse side effects [9]. For that reason, there are several approaches to develop systems allowing accelerated and increased osseointegration of implants by local release of strontium. Studies have already shown that local release of Sr^{2+} ions, e.g. from strontium-functionalized titanium implant surfaces, increases the volume and microarchitecture of bone tissue around the implants. Thereby, both implant fixation and osseointegration are improved [7,10].

In addition to titanium implants, calcium phosphate cements (CaP) are used as bone replacement materials in fracture healing. CaP cements have a chemical similarity to natural bone mineral phase, possess excellent biocompatibility and are both resorbable and osteoconductive [11–15]. They also enable the release of therapeutic agents right at the bone fracture site and thus limit drug release to the fracture area. It was shown *in vitro* that incorporation of strontium into CaP leads to inhibition of osteoclastic resorption as well as stimulation of osteoblast-like cells [11,16]. Furthermore, strontium-doped CaPs accelerate the fracture healing process of osteoporotic bone by increasing bone formation *in vivo* [12,17].

Properties and characteristics of local drug release from such cements as well as drug mobility in bone tissue play an important role in the development and evaluation of new biomaterials. Ideally, the active ingredient should be released over a certain period in a constant dose. The drug concentration in the surrounding tissue should be slightly above the effective threshold. In numerous studies, the release behavior of active substances from biomaterials into water, cell culture medium or simulated body fluid is investigated [18–20].

However, for practical and technical reasons, it is a challenge to follow the kinetics of drug release, spreading and degradation of implant materials *in vivo*. With the analytical methods typically used in pharmaceutical studies, it is not possible to detect substances spatially resolved in bone. Furthermore, active ingredients are often administered in small doses and most imaging methods require high concentrations of the substances. This might be one reason for the deficit in the description of drug release from bone replacement materials and their transport in bone in the current literature.

In two studies of Giers *et al*. [21] and McLaren *et al*. [22], drug detection has been achieved *in vivo* by magnetic resonance imaging (MRI). One drawback of this method is that both the concentration of the drug and the contrast agent chemically bound to the drug as a marker must be very high for MRI. A second drawback is the marker itself because it can significantly influence the drug distribution behaviour.

Post-mortem examination of bone samples is another way to estimate and map drug distribution using analytical methods. Most promising detection methods are mass spectrometry imaging methods like time-of-flight secondary ion mass spectrometry (ToF-SIMS) [23]. ToF-SIMS is currently the only mass spectrometry imaging technique that allows simultaneous detection of organic and inorganic substances in trace concentrations with a spatial resolution down to 100 nm [24]. Owing to its high sensitivity and high-resolution imaging capability, ToF-SIMS has already been used in numerous studies for analysis of bone formation, biomaterial–protein interactions or implant–tissue interactions [12,25–27].

In a recent study, we successfully determined the Sr^{2+} diffusion coefficients for healthy and osteoporotic trabecular bone by ToF-SIMS depth profiling [28]. These experimentally obtained parameters were used to perform a simple simulation of drug release and mobility in bone by finite-element calculation. Other parameters necessary for the simulation, like diffusion coefficients for cortical bone or bone marrow, were only estimated. Therefore, our current study is a follow up based on our previous study aiming to investigate Sr^{2+} diffusion in cortical rat bone.

For assessment of new functionalized bone cements, the determination of spatially resolved drug distribution and concentration in bone is essential. In general, quantification using ToF-SIMS is quite challenging. The ionization process as well as secondary ion yields strongly depend on the chemical and physical environment of the elements and molecules in the sample [29–31]. This so-called matrix effect stands for the variability of ion yields of the same analyte in different chemical environments. Therefore, appropriate standards that possess a nearly identical composition as the analysed material are required. Henss *et al*. [29] showed successful quantification of calcium in bone by ToF-SIMS, using standards with an almost identical composition as natural bone.

In the present paper, we focus on Sr^{2+} transport properties in healthy and osteoporotic cortical rat bone. Therefore, the diffusion coefficient of Sr^{2+} in cortical bone is determined experimentally by classical ToF-SIMS depth profiling. For elucidation of cortical bone nano- and ultrastructure, we performed transmission electron microscopy (TEM) investigations. Furthermore, we prepared and established mineralized collagen standards for ToF-SIMS quantification of Sr^{2+} content in bone sections. The aim of this study is to determine further parameters for the mobility and spreading of Sr^{2+} in bone. Together with our previous study, these parameters could be used for a three-dimensional simulation of the dispersion of Sr^{2+} from functionalized bone implants. The application of these three-dimensional simulations as prediction tool in the development and evaluation of new biomaterials might help to reduce animal tests in the future.

2. Experimental procedure

2.1. Preparation of bone samples

All interventions were performed in full compliance with the institutional and German protection laws and approved by the local animal welfare committee (reference number: V 54-19 c 20-15 (1) GI 20/28 No. 108/2011). Ten-week-old healthy female Sprague–Dawley rats were purchased from Charles River (Sulzfeld, Germany), with an initial weight of 250–290 g. All animals were randomly assigned to two different treatment groups: either SHAM ($n = 10$) operated or ovariectomized (OVX, $n = 20$). Animals underwent an acclimatization period of four weeks before induction of osteoporotic bone status to the OVX group by bilateral ovariectomy combined with a calcium-, phosphorus- and vitamin D3-, soy- and phytoestrogen-free multi-deficient diet (Altromin-C1034, Altromin Spezialfutter GmbH, Lage, Germany) (electronic supplementary material, table S1) as previously described [17,32]. SHAM operation consisted of laparotomy without ovariectomy and thereafter, SHAM animals received a standard rat diet (Altromin-C100, Altromin Spezialfutter

GmbH, Lage, Germany) (electronic supplementary material, table S1).

pS100 was used as the biomaterial, pS100 is the paste variant of the strontium-substituted cement S100 which is described in previous studies [11,25]. A strontium-substituted cement precursor was prepared according to [11]. Afterwards, the precursor powders were mixed with 2.5 wt% finely grounded K_2HPO_4 and dispersed in a carrier liquid consisting of Miglyol 812 with 14.7 wt% Cremophor ELP (BASF) and 4.9 wt% Amphisol A (Brenntag AG) according to [33] resulting in a paste-like strontium-containing cement. Characterization of pS100 is described in [34].

For pS100 material implantation, a wedge-shaped osteotomy was performed on the distal end of the left femur after 12 weeks of osteoporosis induction (previously described in [17], only for the OVX group). The distal femur was fixed laterally with a seven-hole T-shaped mini-plate (Leibinger® XS-miniplate, Stryker, Schönkirchen, Germany). Afterwards, a wedge-shaped defect with lateral length of 4 mm and medial gap of 0.35 mm was created in the distal metaphyseal area using an ultrasound bone saw (Piezosurgery® 3, Saw blade OT7S-3, Mectron, Köln, Germany). The defect was either filled with pS100 or left empty (control group) ($n = 10$ animals, respectively) and allowed to heal six weeks before euthanasia.

All animals were euthanized 18 weeks post-ovariectomy under inhalation of CO_2 after general anaesthesia. Right femurs of SHAM and OVX as well as left femurs of the OVX group with biomaterial and empty defect were harvested. All surrounding soft tissue was removed. Femurs were fixed in 4% formalin and dehydrated in a series of alcohol gradient xylol before final embedding in methylmethacrylate (Technovit 9100; Heraeus Kulzer, Hanau, Germany). Right femurs without biomaterial were cut into sections of 20–50 µm thicknesses and ground before further analysis.

Technovit blocks of left femurs with implanted biomaterials and empty defect were sectioned into 5 µm thick slices with the aid of Kawamoto's film (Section-Lab Co. Ltd, Japan) to keep the biomaterials intact. For mass spectrometry analysis, sections were deplastified with 2-methoxyethyl acetate (MERCK, Germany) triple for 20 min each and dried before further analysis. For quantification of Sr^{2+} content in rat bone, one bone section of each of three animals of the empty defect (control) group and one bone section of each of four animals of the pS100 group were analysed.

2.2. Dipping experiment

Ground bone sections of right femurs were fully immersed in 1 mol l^{-1} strontium chloride solution for 10 min, rinsed afterwards with Milli-Q® water and air-dried. A high concentration was chosen in order to get good statistics in the following mass spectrometric analysis. ToF-SIMS depth profiling was carried out on one bone section of each of three healthy (SHAM) and three osteoporotic (OVX) animals. Therefore, on each sample, three depth profiles were carried out in the centre area of cortical bone.

2.3. Collagen standards

According to a method of simultaneous collagen fibril reassembly and mineralization developed by Bradt *et al.* [35], membranes from biomimetic mineralized collagen (tapes) were prepared as described in [36]. Briefly, acid-soluble collagen type I isolated from calf skin (Collaplex 1.0, GfN, Germany) was dissolved in 10 mM hydrochloric acid. To generate a standard curve, the collagen solution was then mixed with either 0.1 M $CaCl_2$ (Sr-free tapes) or with defined combinations of 0.1 M $CaCl_2$ and 0.1 M $SrCl_2$ solutions (4, 3, 2, 1, 0.75, 0.5 wt% Sr-modified tapes). The pH was adjusted to 7.0 using 0.5 M TRIS (pH 11) and 0.5 M Sørensen phosphate buffer (pH 7.4), allowing the simultaneous collagen fibril reassembly and precipitation of nanocrystalline hydroxyapatite and Sr-containing mineral phases during an incubation at 37°C for 12 h. The precipitate consisting of about 30 wt% collagen and 70 wt% mineral phase was collected by centrifugation and resuspended in distilled water (1 g collagen per 100 ml). To prepare the membrane-like tapes, mineralized collagen was condensed by vacuum filtration using a porous G4 glass filter frit (Schott, Germany). The densified material was then cross-linked by a 1% aqueous solution of *N*-(3-dimethylaminopropyl)-*N*-ethylcarbodiimide hydrochloride for 1 h, rinsed thoroughly in distilled water, in 1% glycine solution and once again in water. For the present study, circle-shaped samples with a diameter of 12 mm were cut from the material before they were frozen at −20°C and freeze-dried.

2.4. Inductively coupled plasma optical emission spectrometry

Inductively coupled plasma optical emission spectrometry (ICP-OES, iCAP 6500 Duo View, Thermo Fisher Scientific, USA) was used for chemical element analysis of the mineral phase of the Sr-substituted tapes. Therefore, the tapes ($n = 3$ of each group) were dissolved in 0.45 ml 65% HNO_3 (Merck, Germany) for 10 min at room temperature, while shaking at 400 min^{-1}. The digested solution was then diluted with ultrapure water to 15 ml and filtered using 0.45 µm polypropylene (PP) syringe filter (VWR International, USA). The concentrations of Ca^{2+}, Sr^{2+} and PO_4^{3-} were determined after calibration with data from element standards (High Purity, USA) measured in bracketing mode.

2.5. Time-of-flight secondary ion mass spectrometry

ToF-SIMS measurements were carried out in the positive ion mode with a ToF-SIMS 5–100 machine (IonToF GmbH, Münster, Germany) equipped with a bismuth cluster primary ion source (25 keV) and Cs, O_2 and Ar_x sputter guns. Depth profiling of cortical bone of ground samples, collagen standards and bone cross-sections was performed in the non-interlaced mode. The sample surface was in each case analysed in an area of 75×75 µm^2 with 25 keV Bi_3^+ ions as analysis species. The primary ion gun was operated in the spectrometry (low-current bunched) mode with 60 µs cycle time, 128×128 pixel with 1 shot/pixel and a current of about 0.3–0.5 pA. The obtained mass resolution $m/\Delta m$ full width at half maximum was for all measurements better than 4000 for the Ca^+ mass signal. Some depth profiles were analysed in the delayed extraction mode with the following parameters: 256×256 pixel, 5 shots/pixel, 10 frames with a delay time of 0.075–0.125 µs and a current of 0.06–0.09 pA. After each analysis scan, the sample surface was sputtered for 10 s with 1 keV O_2^+ ions. Sputter beam area was 170×170 µm^2 centred on the analysis area to avoid edge effects.

The sputter current was between 290 and 340 nA. Charge compensation was done with a low-energy electron flood gun. After depth profiling, the depth of each sputter crater was measured with a confocal microscope PLu neox 3D (Sensofar, Terrassa, Spain) to calibrate the sputter time axis. Data analysis of the ToF-SIMS measurements was done with Surface Lab Software version 6.8 (IonToF GmbH).

For Sr^{2+} quantification, six to nine depth profiles were measured of each prepared standard (three depth profiles per tape, two to three tapes per standard concentration). Measurements were taken on different areas of $75 \times 75\ \mu m^2$ with 128×128 pixel, 1 shot/pixel and 150 scans. The mean values for Sr^+ signal intensities were divided by the sum of the mean values for the Sr^+ and Ca^+ signal intensities. Owing to linear dependence of $Sr^+/(Sr^+ + Ca^+)$ from the Sr^{2+} content of the standard tapes, a linear fit was reasonable.

Overview two-dimensional images of whole bone sections were obtained by the so-called stage scans in the spectrometry (low-current bunched) mode with the following parameters: 10 shots/pixel, rastered in sawtooth mode, 10 frames per patch, cycle time 55 µs and three scans. The obtained mass resolution $m/\Delta m$ was for all measurements better than 3000 for the Ca^+ mass signal. More detailed images of smaller areas were taken in the delayed extraction mode: 512×512 pixel, 10 shots/pixel, 50 scans (1024×1024 pixel, 1 shots/pixel, 100 scans) with a delay time of 0.135 µs and a current of 0.08–0.1 pA. More detailed information on SIMS measurements of bone is described in [26,37].

2.6. Transmission electron microscopy

To prepare the electron-transparent TEM specimen of cortical bone, the focused ion beam technique was used. In the first step, a thin lamella of a thickness of about 1 µm is exposed by a focused gallium ion probe (energy: 30 eV) in a Zeiss Cross Beam 1540 XB (Oberkochen, Germany). After welding of this lamella onto a special girder, it was finally thinned by the gallium ion probe with lower energy (5 keV) until a thickness less than 100 nm is reached. The complete sample processing is done under scanning electron microscopic control. A protection bar of hydrocarbon with platinum is deposited onto the sample before starting the procedure in order to minimize the amorphization.

The transmission electron microscopic analyses were done using an FEI TEM/STEM microscope Tecnai F30 ST (Eindhoven, The Netherlands). The accelerating voltage used during the measurements was 300 kV reaching a resolution limit of better than 0.2 nm. TEM analysis was carried out with samples of one healthy (SHAM) and one osteoporotic (OVX) animal.

2.7. Quantification of collagen fibrils using FibrilTool

Quantification of collagen fibrils regarding their anisotropy and average fibril array orientation was applied using the ImageJ plugin FibrilTool. FibrilTool quantifies collagen fibrils in a region of interest (ROI) of a high-resolution TEM (HRTEM) image using ImageJ software (ImageJ version 2.4, National Institutes of Health, Bethesda, MD, USA). The concept of nematic tensor approach from liquid crystals is used to quantify the main orientation of fibrillary structures in the analysed image [38,39]. The output is a statement about how the fibrils are aligned and are computed on the basis of pixel intensity level in the selected ROIs. Under the presumption that fibrils favour a definite orientation along a given axis, fibrils are considered isotropic when no alignment is seen (scored with zero), whereas perfectly arranged fibrils are considered anisotropic (scored with one).

2.8. Statistical analysis

Differences in diffusion coefficients were analysed using the Mann–Whitney *U*-test after ascertaining a non-normal distribution with a Shapiro–Wilk test. Diffusion coefficients are reported as means ± s.e.m. Collagen fibre properties obtained using FibrilTool were analysed using two-way ANOVA test accompanied by two-sample *t*-test. The same statistical analysis was used for quantification of Sr^{2+} in rat bone cross-sections. A value of $p < 0.05$ was regarded as significant. Statistical analyses were performed using Origin v9.3 (OriginLab Corporation, Northampton, MA, USA).

3. Results

3.1. Determination of Sr^{2+} diffusion coefficient in cortical bone

The diffusion coefficient of Sr^{2+} in healthy and osteoporotic cortical bone tissue was experimentally determined by ToF-SIMS. Therefore, bone cross-sections of rat femur were dipped in aqueous Sr^{2+}-solution by one side. Afterwards, Sr^{2+} distribution in mineralized bone tissue was measured by classical ToF-SIMS depth profiling. In ToF-SIMS, secondary ions (e.g. elements, molecule fragments) are mostly single charged despite their original chemical nature. For this work, it can be assumed that the detected Sr^+ ions originate from Sr^{2+} ions in the bone sample. In the first row of figure 1, mass spectrometric images of Ca^+ and Sr^+ distribution in healthy (left) and osteoporotic (right) rat bone sections are shown. Both mass images of the healthy bone section reveal the typical bone structure with a thick layer of cortical bone forming the shell and the trabecular network in the inner area. The osteoporotic bone section was another cutting level and therefore, mass images of Ca^+ and Sr^+ showed only the cortical bone shell. In the second row of figure 1, image cut-out enlargements with higher lateral resolution are depicted. Small cracks are visible that were formed during vacuum treatment in the ToF-SIMS main chamber. These optical artefacts have no influence on the main experiment. Three-dimensional mass data of the marked cortical bone areas of row 2 are shown in the third row. The spatial Ca^{2+} distribution was nearly homogeneous in both healthy and osteoporotic cortical bone, while for Sr^{2+}, a concentration gradient with several fast diffusion paths was observed.

Diffusion coefficients of Sr^{2+} in cortical rat bone were calculated from ToF-SIMS data of depth profiles. Therefore, data evaluation was carried out by fitting a suitable mathematical solution of Fick's second law of diffusion (equation (3.1)) to the experimental data. As boundary conditions for solving Fick's second law of diffusion, we assumed diffusion from an exhaustless source into semi-infinite space [40]. Owing to the proportionality between species concentration and secondary ion intensity in SIMS, the fit can be carried out with the obtained signal intensities.

$$c(x) = c_{bg} + c_0 \cdot \left(1 - \mathrm{erf}\frac{x - x_0}{2\sqrt{Dt}}\right), \tag{3.1}$$

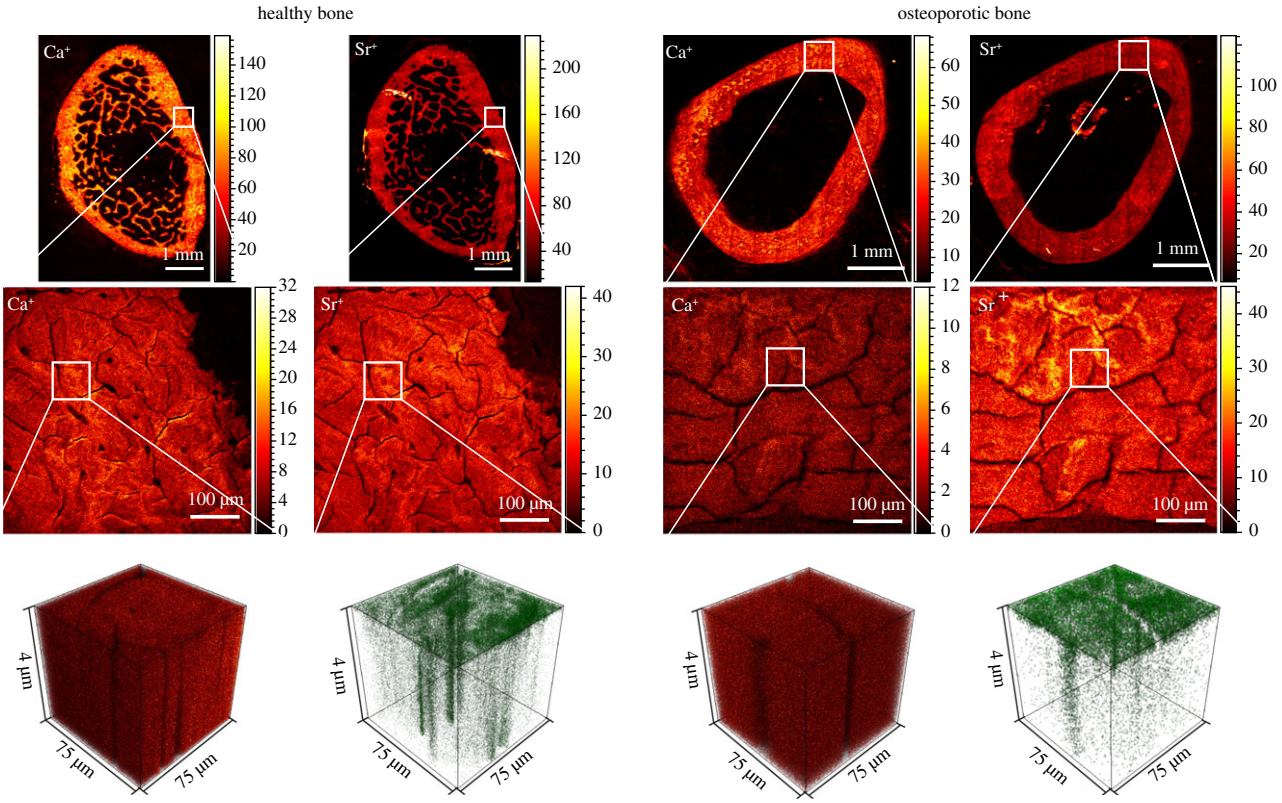

Figure 1. ToF-SIMS data of healthy and osteoporotic cortical bone. Overview mass images show the distribution of Ca^+ and Sr^+ (row 1, stage raster mode) signal. Image sections with higher lateral resolution show the typical cortical bone structure (row 2, delayed extraction mode). Row 3 depicts three-dimensional mass spectrometry data of the marked areas of row 2 with nearly homogeneous Ca^{2+} distribution compared to Sr^{2+} concentration gradient with fast diffusion paths (delayed extraction mode). Twenty-five kiloelectronvolt Bi_3^+ primary ions were used for ToF-SIMS imaging, for sputtering, a 1 keV O_2^+ beam was used.

where c_{bg} is the background concentration of Sr^{2+}; c_0 is the concentration of the infinite source; x is the position/depth; x_0 is the starting point of the diffusion profile; D is the diffusion coefficient; t is the diffusion time.

The mass spectrometric information of each analysis layer was summed up and plotted as a diffusion profile. Figure 2 shows exemplarily intensity versus depth diffusion profiles for healthy and osteoporotic corticalis obtained from ToF-SIMS depth profiling. In SIMS depth profiles, the first data points are commonly influenced by variable dopant concentrations of both primary and sputter ions. Besides that, contamination of the sample surface also occurs. This resulted in an unsteady matrix with non-reliable secondary ion data. For that reason, the first data points of the diffusion profile were skipped for fitting equation (3.1) to the experimental obtained data. Owing to the homogeneous Sr^+ intensity within the fast diffusion channels, these data contribute to the background signal c_{bg} and do not influence the calculated diffusion coefficient.

For healthy cortical bone, we obtained an average diffusion coefficient of $D_{healthy} = (1.68 \pm 0.57) \cdot 10^{-13}\ cm^2\ s^{-1}$. The average diffusion coefficient for osteoporotic cortical bone was $D_{OVX} = (4.30 \pm 1.43) \cdot 10^{-13}\ cm^2\ s^{-1}$ (figure 3). Statistical evaluation did not reveal any significant difference between the diffusion coefficient of Sr^{2+} in healthy and osteoporotic cortical bone.

3.2. Structure of cortical bone

To characterize the nano- and ultrastructure of healthy and osteoporotic cortical bone different modes and methods were applied: high annular darkfield (HAADF) imaging in scanning transmission TEM (STEM) mode, TEM brightfield (BF) imaging, electron diffraction (ED) and HRTEM imaging including Fourier transformation (FT) of the HRTEM images (figure 4).

STEM images, as well as the TEM-BF images, depicted mostly lamellar and irregular structures with no significant structural differences between healthy and osteoporotic bone. In STEM-HAADF images, the 65 nm periodicity typical for mineralized collagen fibrils can be seen. ED patterns revealed that calcium hydroxyapatite (HAP) is the dominant phase in the images of both healthy and osteoporotic cortical bone. In HRTEM images, the strip-type arrangement of hydroxyapatite was visible with the (100) and (112) lattice planes of HAP with distances of 0.82 nm and 0.28 nm, respectively. The c axis was oriented parallel to the collagen fibrils in the mineralized areas of healthy as well as osteoporotic cortical bone with no significant differences between the two groups.

HRTEM images of healthy and cortical rat bone were computationally segmented using FibrilTool. Both anisotropy and average fibril orientation (figure 5) of collagen fibres were slightly higher in healthy cortical bone than in osteoporotic cortical bone. However, the differences were not statistically significant.

3.3. Quantification of Sr^{2+} content in bone

ToF-SIMS analysis of strontium-substituted mineralized collagen standards showed mass signals of hydroxyapatite, e.g. Ca^+ (39.97 m/z), $CaPO_2^+$ (102.94 m/z), $Ca_2PO_3^+$ (158.91 m/z), $Ca_2PO_4^+$ (174.91 m/z) and collagen, $C_4H_8N^+$ (70.0 m/z)

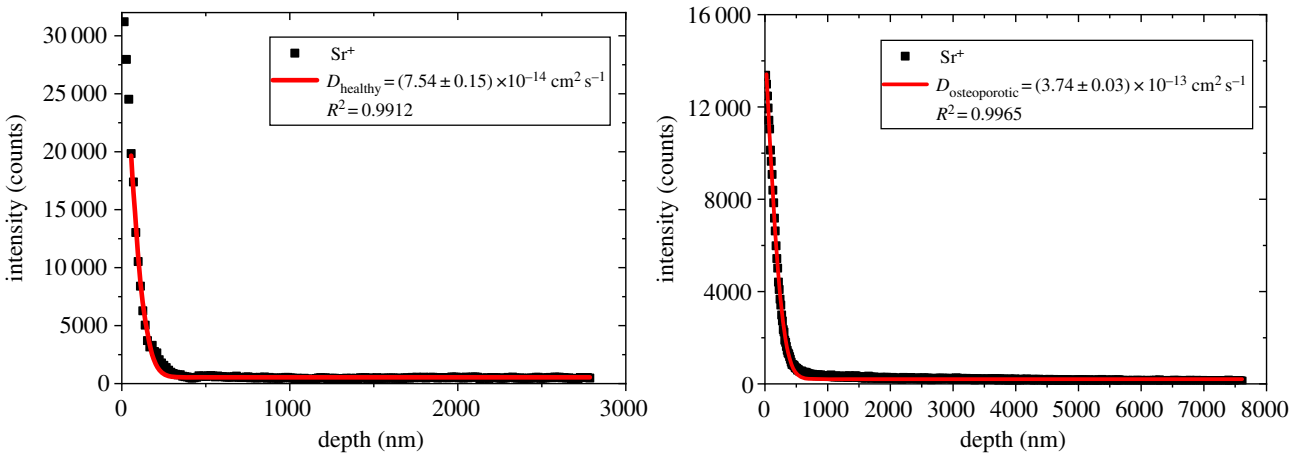

Figure 2. ToF-SIMS depth profiles of Sr^+ in healthy (left) and osteoporotic (right) cortical bone. To obtain the diffusion coefficient, diffusion from an exhaustless source into semi-infinite space was assumed. The solid line is in each case the result of the performed fit according to equation (3.1). Sputtering was done with a 1 keV O_2^+ ion beam, for analysis, Bi_3^+ primary ions were used.

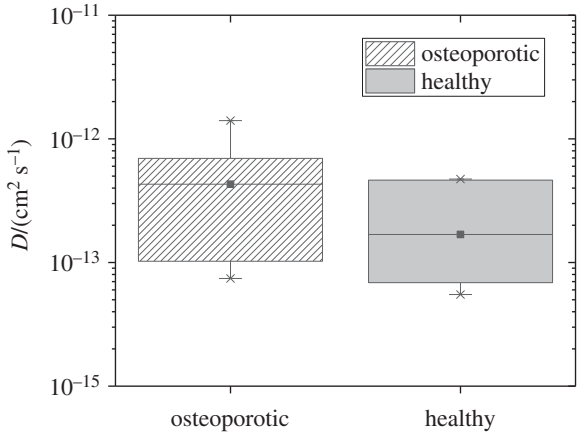

Figure 3. Experimentally obtained diffusion coefficients (D) of osteoporotic and healthy cortical bone. For both osteoporotic and healthy cortical bone, $n = 9$ samples (one bone sample of three animals each from each group, on each bone sample, three depth profiles) were analysed. The mean diffusion coefficient for healthy cortical bone differs only slightly from the mean diffusion coefficient for osteoporotic bone (Mann–Whitney test).

[26,29]. These characteristic peaks and fragmentation patterns of collagen and HAP were also obtained from mineralized bone tissue.

For Sr^{2+} quantification in collagen standards, depth profiles were measured of each prepared standard. The plot of the obtained signal intensities of $Sr^+/(Sr^+ + Ca^+)$ versus Sr^{2+} content in collagen standard tapes resulted in a linear relationship (figure 6*a*). The actual strontium content of the collagen standards was determined using ICP-OES. The large error bars are partly due to rough surfaces of the collagen standards, which influences the signal intensity.

Bone cross-sections of rat femurs from two different animal groups (empty defect, pS100) were analysed. pS100 is the paste variant of the Sr^{2+}-enriched calcium phosphate cement S100 [11,13,41]. For S100, successful release of Sr^{2+} and locally induction of new bone formation *in vivo* was already shown [12].

Two-dimensional ToF-SIMS images of whole bone sections are shown exemplarily in figure 7*a*,*b*. They were obtained by the so-called stage scans in the spectrometry mode. ToF-SIMS mass images are overlays of Ca^+ (red), $C_4H_8N^+$ (green) and Sr^+ (blue). Cortical and trabecular bone structure surrounded by unmineralized collagen bone tissue is clearly shown in both groups. Additionally, fragmentation of pS100 cement can be seen. Strontium was detected in rat bone sections of pS100 in the remaining bone cement, biomaterial/tissue interface regions and up to 4–6 mm from the implant area (figure 7*d*).

For determination of Sr^{2+} content, strontium distribution in bone sections (n(animals) = 3 control, n(animals) = 4 pS100, one bone section from each animal) in cortical bone (cb), cortical bone near biomaterial (cb nb) as well as trabecular bone (tb) was measured by ToF-SIMS depth profiling under the same measurement conditions as the collagen standards. For each bone section and each region, two depth profiles were measured. Applying the obtained calibration curve of figure 6*a*, the quantitative determination of Sr^{2+} content in bone sections is possible. The results are shown in figure 7*c*.

4. Discussion

Our present study provides new insights into Sr^{2+} transport properties in bone. We demonstrate that Sr^{2+} diffusion in healthy cortical rat bone does not differ from Sr^{2+} diffusion in osteoporotic cortical rat bone. Moreover, we establish standards for Sr^{2+} quantification in rat bone by ToF-SIMS.

In our study, two-dimensional ToF-SIMS images of healthy bone reveal the typical bone structure with a thick layer of cortical bone forming the shell and the trabecular network in the inner area (figure 1), as described in the literature [42]. In both healthy and osteoporotic cortical bone, we obtain three-dimensional mass data which show nearly homogeneous Ca^{2+} distribution, while for Sr^{2+}, a concentration gradient with several fast diffusion paths can be observed (figure 1). These fast diffusion paths in cortical bone are possibly Haversian canals or osteocyte networks and need to be further investigated [42,43].

For determination of Sr^{2+} diffusion coefficients in healthy and osteoporotic cortical rat bone, we fitted the solution of Fick's second law for diffusion into semi-infinite space with ToF-SIMS depth profile data. Minor deviations between experimental and theoretical data are due to the complex bone morphology of cortical bone which is a natural tissue and therefore different from individual to individual. These differences can be seen in two-dimensional and three-dimensional ToF-SIMS images (figure 1).

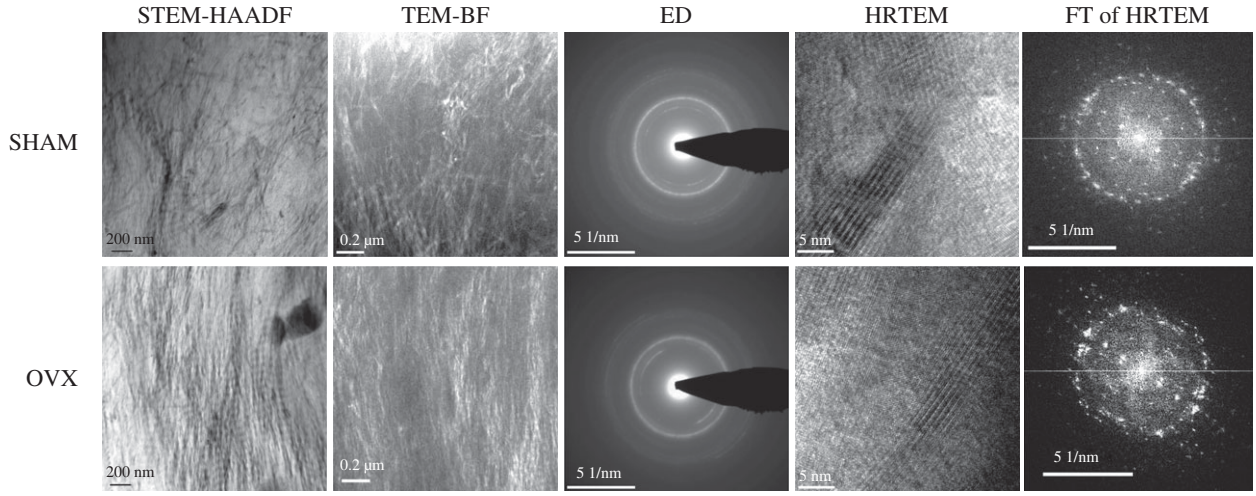

Figure 4. Comparison of the nano- and ultrastructure of healthy and osteoporotic cortical rat bone investigated by TEM. In STEM-HAADF images, the 65 nm periodicity typical for mineralized collagen fibrils can be seen. In HRTEM images, the strip-type arrangement of hydroxyapatite is visible. FT of HRTEM images was applied to quantify the mean collagen orientation. There were no significant differences between healthy and osteoporotic rat bones. $n = 7$ TEM lamella were analysed from each group.

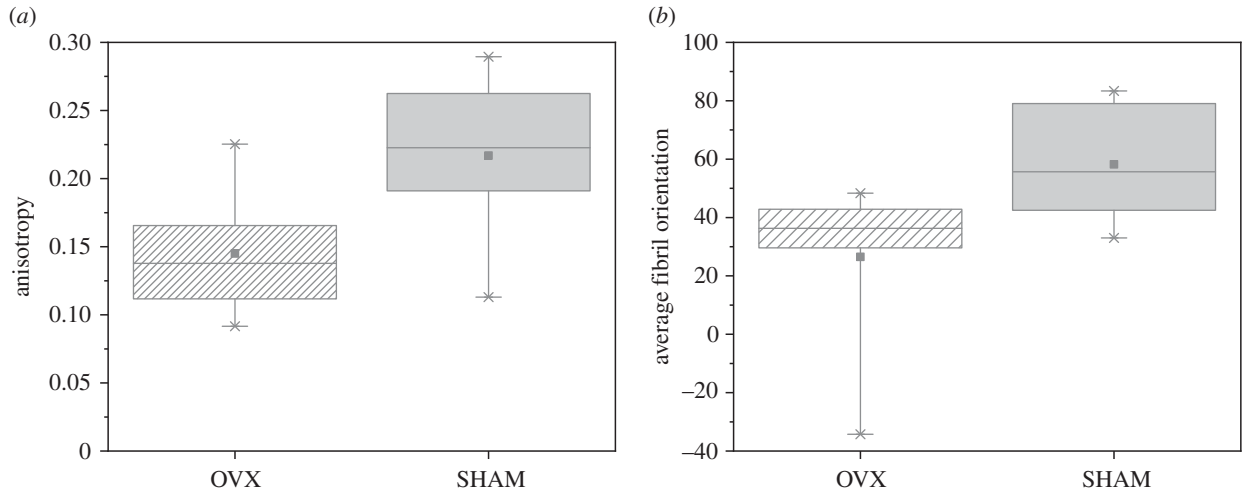

Figure 5. Collagen fibre properties of OVX and SHAM cortical rat bone obtained using FibrilTool. OVX and SHAM showed no statistically significant differences in fibril anisotropy (*a*) and fibril orientation (*b*) (two-way ANOVA test accompanied by two-sample *t*-test). For both osteoporotic and healthy cortical bone, $n = 6$ HRTEM images were analysed, respectively.

For healthy cortical rat bone, we obtain a diffusion coefficient of $D_{\text{healthy}} = (1.68 \pm 0.57) \cdot 10^{-13}\ \text{cm}^2\ \text{s}^{-1}$. This value differs only slightly from the value of $D_{\text{OVX}} = (4.30 \pm 1.43) \cdot 10^{-13}\ \text{cm}^2\ \text{s}^{-1}$ for osteoporotic cortical bone. Statistical data evaluation did not reveal any significant difference between the diffusion coefficient of Sr^{2+} in healthy and osteoporotic cortical bone. The reason for the relatively large errors of the diffusion coefficients is due to the fact that the experimental data were obtained from cortical bone from three different animals of each group. As said before, bone is a natural tissue with a complex morphology and differs from individual to individual. Nonetheless, these results indicate a comparable bone nanostructure for both types of cortical bone status. Here, we used TEM for the investigation of cortical bone nanostructure from the diaphysis of healthy and osteoporotic rat femur. As expected from our experimentally obtained diffusion coefficients, TEM images and computational segmentation of collagen fibrils using FibrilTool show no significant difference between healthy and osteoporotic cortical bone.

In a recently published study, we investigated Sr^{2+} transport in trabecular bone [28]. Trabecular bone is present within or at the ends of long bones and shows less density, less homogeneity as well as a lesser degree of parallel orientation of lamellae than cortical bone [44]. In contrast with our present study, in trabecular bone, the diffusion coefficient $D_{\text{OVX,tr}} = (1.55 \pm 0.93) \cdot 10^{-10}\ \text{cm}^2\ \text{s}^{-1}$ for osteoporotic bone was two magnitudes higher than the diffusion coefficient of healthy bone, $D_{\text{healthy,tr}} = (2.28 \pm 2.97) \cdot 10^{-12}\ \text{cm}^2\ \text{s}^{-1}$. This significant difference was correlated with different trabecular bone nanostructure, which was observed by focused ion beam scanning electron microscopy and TEM.

Osteoporosis is generally defined as loss of bone mass. Nonetheless, previous studies revealed differences in osteoporotic bone loss between trabecular and cortical bone [44–46]. In both cases, osteoporotic bone loss is a response to an imbalance in bone remodelling. In healthy bone, amounts of removed and replaced bone tissue during bone remodeling are equal to each other. In osteoporosis, bone resorption is faster than new bone formation, thus disturbing

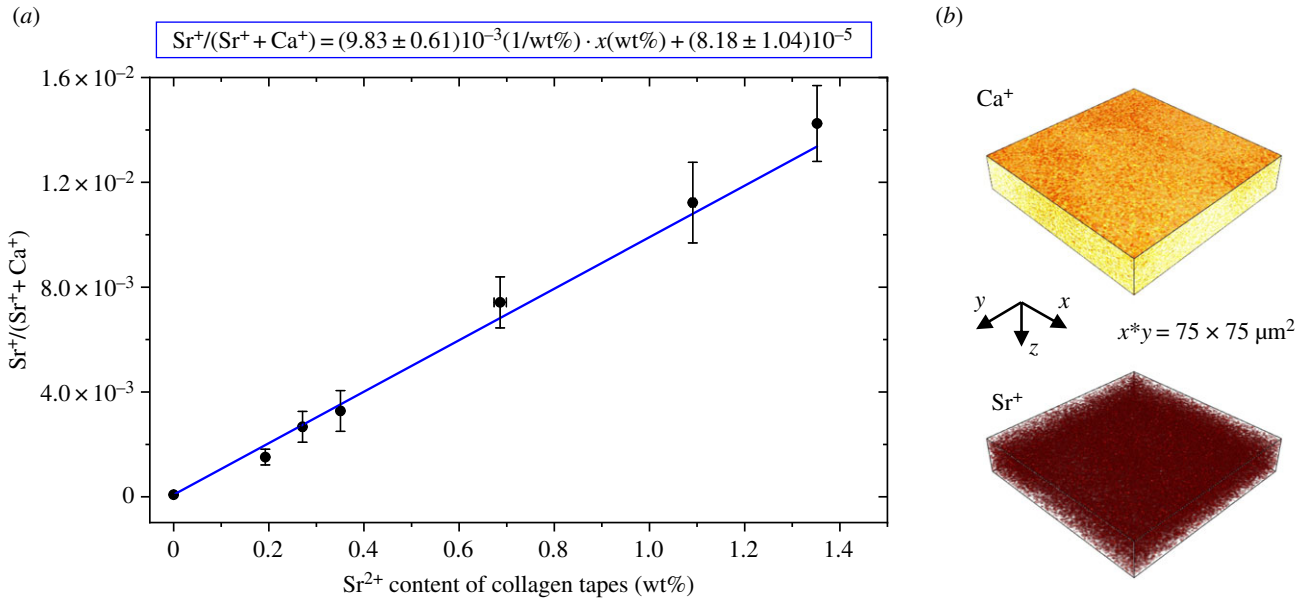

Figure 6. ToF-SIMS data from strontium-containing mineralized collagen tapes. (*a*) Linear dependence of $Sr^{+}/(Sr^{+} + Ca^{+})$ from Sr^{2+} content of standard tapes. Linear fit and linear equation are shown. (*b*) Three-dimensional rendered plots of Ca^{+} and Sr^{+} signal of a strontium-containing mineralized collagen tape (exemplarily 3 wt% strontium substitution), which served as standard for Sr^{2+} quantification in bone. A 1 keV O_2^{+} beam was used for sputtering; analysis was carried out with 25 keV Bi_3^{+} as primary ion species. Ca^{+} and Sr^{+} are distributed homogeneously within the material.

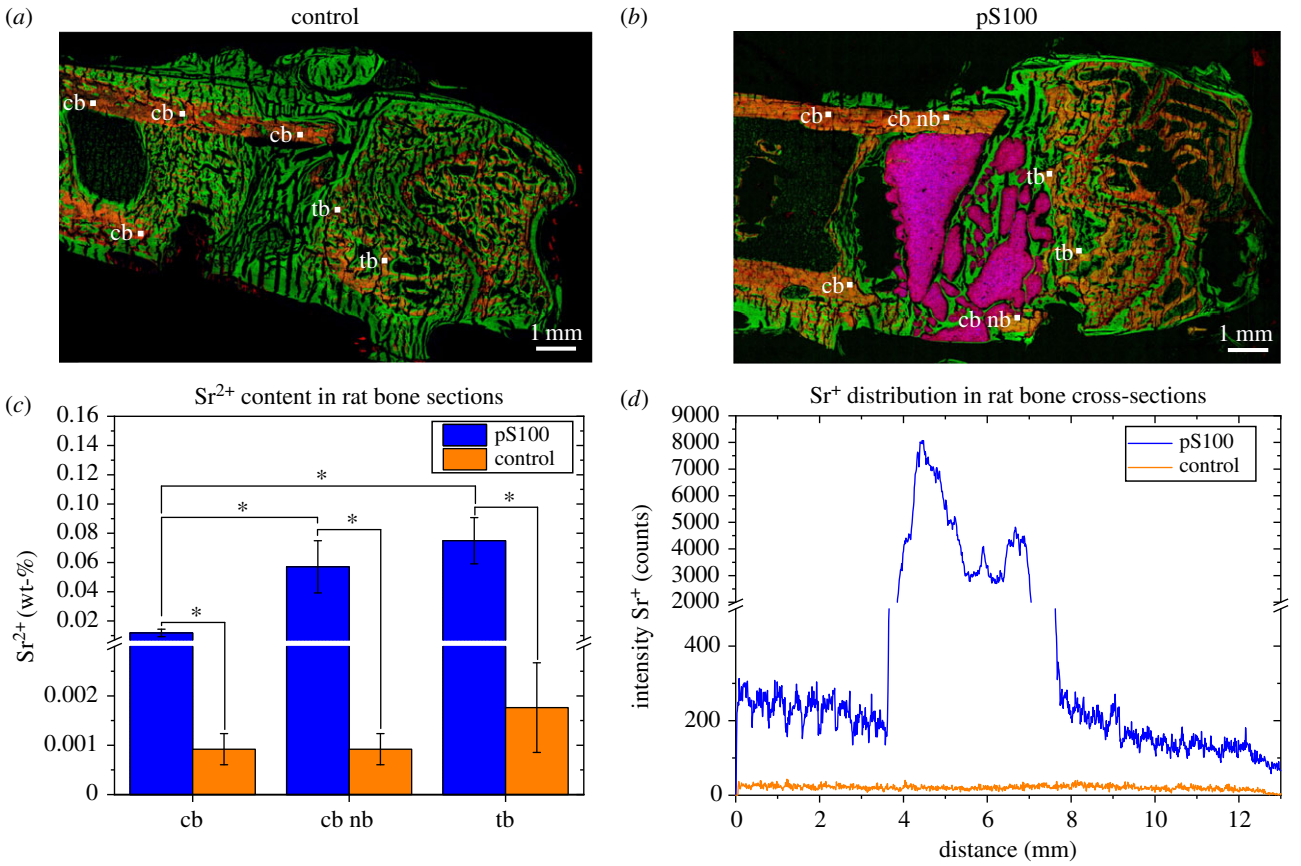

Figure 7. Determination of Sr^{2+} in rat bone cross-sections. ToF-SIMS images of rat femur sections of (*a*) control and (*b*) pS100 group showing overlays of Ca^{+} (mineralized bone, red), $C_4H_8N^{+}$ (collagen fragment, green) and Sr^{+} (blue). (*c*) Results for the quantification of the strontium content in rat bone sections with (pS100) and without (control) biomaterial. Measured regions are labelled as follows: cb, cortical bone; cb nb, cortical bone near biomaterial (only pS100 group); tb, trabecular bone. The mean values and the standard deviation of the mean values are depicted. The asterisks indicate the significance level (*$p < 0.05$, $n = 8$ for each region of pS100, $n = 6$ for each region of control, two-way ANOVA test accompanied by two-sample *t*-test). (*d*) Sr^{2+} distribution in bone sections shows concentration gradient from biomaterial pS100 to enclosing bone tissue. Empty defect shows natural Sr^{2+} occurrence in bone and serves as control.

the remodelling balance [1,44,47]. Bone remodelling takes place on osseous surfaces. Therefore, bone loss can be displayed as a function of surface availability for bone turnover. Compared to cortical bone, trabecular bone possesses a high surface-to-volume ratio. Thus, the remodelling rate of trabecular bone is much higher than for cortical

bone and trabecular bone loss takes place before cortical bone loss [44–46].

In contrast with our previous study of trabecular bone [28], in our current study, there are no significant differences between healthy and osteoporotic cortical bone, neither in drug distribution behaviour nor in bone ultrastructure. Therefore, our results indicate an early stage of osteoporosis in which mainly trabecular bone loss occurred. Moreover, diffusion coefficients for Sr^{2+} in healthy and osteoporotic cortical bone are one magnitude lower than Sr^{2+} diffusion in healthy trabecular bone and three magnitudes lower than Sr^{2+} diffusion in osteoporotic trabecular bone. Together with our results of TEM analysis of cortical bone ultrastructure, this shows a denser bone tissue in cortical bone than in trabecular bone which is in line with [44,48,49].

In the second part of our study, we applied locally resolved quantification of Sr^{2+} in bone sections using ToF-SIMS. Owing to the matrix effect, quantification of concentrations using ToF-SIMS is quite challenging and appropriate standards are required for nearly identical compositions as in the material analysed [29–31]. ToF-SIMS analysis of the collagen standards and bone tissue reveal characteristic peaks and fragmentation patterns of collagen and HAP, which are well known from different ToF-SIMS studies of bone tissue [25,26,29]. This similarity of the chemical composition of bone tissue and collagen standards is essential because the ionization process in ToF-SIMS strongly depends on the chemical environment of surface elements and molecules.

For Sr^{2+} quantification, depth profiles were measured of each prepared standard and a linear correlation of the signal intensities of $Sr^+/(Sr^+ + Ca^+)$ versus Sr^{2+} content within the concentration range of 0–1.4 wt% Sr^{2+} was obtained. This is an important prerequisite for quantification of Sr^{2+} in bone sections. Error bars indicate rather rough surfaces of the collagen standards which influenced signal intensity. Nevertheless, the linear relationship between $Sr^+/(Sr^+ + Ca^+)$ and Sr^{2+} content clearly qualifies the samples as suitable standards within error tolerances for Sr^{2+} quantification in bone.

Bone samples from two different animal groups were obtained six weeks after induction of critical-size metaphyseal fracture defect in the femur of osteoporotic rats according to [12]. In one animal group, the defect was left empty. Therefore, these bone samples served as a control for natural Sr^{2+} occurrence in bone. In the second group, the defect was filled with the Sr^{2+}-enriched calcium phosphate cement paste pS100 [34].

The release of Sr^{2+} from the cement, as well as calcium and collagen mass distribution of bone cross-sections, are studied by ToF-SIMS. In rat bone sections containing pS100 cement, Sr^{2+} is detected in the remaining bone cement and biomaterial/tissue interface regions. Furthermore, strontium enrichment is found up to 4–6 mm from the implant area in trabecular bone and the outer areas of cortical bone oriented to the cement. This demonstrates the successful *in vivo* release of strontium from the bone cement into the bone. Additionally, fragmentation of pS100 is shown. These findings are consistent with a previous study, which demonstrated considerable release of Sr^{2+} from strontium-containing bone cements *in vivo* [12] with enhanced new bone formation clearly associated with the local release of Sr^{2+} from SrCPC. Our data are also in line with [28].

For the first time, we not only studied whether a detectable amount of Sr^{2+} is incorporated into new bone tissue *in vivo* or not but also quantified Sr^{2+} content in bone sections. Measurement of Sr^{2+} content in bone tissue is quite important for determination of the effectiveness of Sr^{2+} release from bone cements. Numerous studies reported strontium incorporation into mineralized bone [5,50]. Hereby, Sr^{2+} is bound on the surfaces of the HAP crystals of old bone and found in higher concentrations in the bulk of newly formed bone [50–52] after oral administration of strontium. Furthermore, Dahl *et al*. [5] found out that the amount of strontium in trabecular bone is higher than that in cortical bone because Sr^{2+} incorporation is influenced by bone turnover. In our present study, we were able to distinguish strontium content of different bone compartments. We found higher amounts of strontium in trabecular bone than in cortical bone. Moreover, Sr^{2+} content in cortical bone close to pS100 cement was higher than Sr^{2+} content in cortical bone somewhat further away from the cement. Therefore, our findings are in line with those of others.

5. Conclusion

This study shows the application of ToF-SIMS to assess Sr^{2+} ion distribution as well as quantification in bone. The results provide important insights regarding the transport properties in healthy and osteoporotic cortical bone. Together with the results of our recently published data, all experimentally obtained parameters can be used to perform a simulation of drug release and mobility in bone by finite-element calculation. Though further studies regarding Sr^{2+} mobility in bone marrow are still necessary, this study contributes to our main goal: three-dimensional simulation of Sr^{2+} mobility in bone using finite-elements calculation. This could be used as a tool for development and evaluation of new biomaterials to predict whether the amount of strontium released by a biomaterial will be sufficient to promote local bone healing. Overall, this might help to reduce animal experiments in the future.

Ethics. All interventions were performed in full compliance with the institutional and German protection laws and approved by the local animal welfare committee (reference number: V 54-19 c 20-15 (1) GI 20/28 no. 108/2011).

Data accessibility. The authors confirm that the data support the findings of this study. Data are exemplarily shown within the article and its electronic supplementary material. Additional data that support the findings of this study are available from the corresponding author upon request.

Authors' contributions. C.K. performed ToF-SIMS analysis, data evaluation and interpretation, and drafted the manuscript. M.Q. synthesized and analysed the collagen standards and edited the manuscript. S.R. performed animal experiment including sample preparation. J.T. and T.G. performed TEM analysis including data interpretation and edited the manuscript. M.S. and M.G. developed, synthesized and characterized the bone cement pS100. V.A. performed the animal experiments. M.R. designed the study, assisted in the experiments' design, data evaluation and revised the manuscript. All authors proofread the manuscript and approved the final version.

Competing interests. We declare we have no competing interests.

Funding. This work was funded by the German Research Foundation (DFG, Collaborative Research Centre Transregio 79—subprojects M5, M4, T2 and Z2). We gratefully acknowledge the financial support within this project.

Acknowledgements. The authors thank Nils Döhner and Yannick Moryson for their support with ToF-SIMS measurements and Stefanie Kern for her support with statistical evaluation. We are grateful to Andrea Voß (Leibniz-Institute for Solid State and Materials Research IFW Dresden, Germany) for ICP-OES analysis.

References

1. Rachner TD, Khosla S, Hofbauer LC. 2011 Osteoporosis: now and the future. *Lancet* **377**, 1276–1287. (doi:10.1016/S0140-6736(10)62349-5)
2. Saidak Z, Marie PJ. 2012 Strontium signaling: molecular mechanisms and therapeutic implications in osteoporosis. *Pharmacol. Ther.* **136**, 216–226. (doi:10.1016/j.pharmthera.2012.07.009)
3. Maimoun L, Brennan TC, Badoud I, Dubois-Ferriere V, Rizzoli R, Ammann P. 2010 Strontium ranelate improves implant osseointegration. *Bone* **46**, 1436–1441. (doi:10.1016/j.bone.2010.01.379)
4. Takahashi N, Sasaki T, Tsouderos Y, Suda T. 2003 S 12911-2 inhibits osteoclastic bone resorption *in vitro*. *J. Bone Miner. Res.* **18**, 1082–1087. (doi:10.1359/jbmr.2003.18.6.1082)
5. Dahl SG, Allain P, Marie PJ, Mauras Y, Boivin G, Ammann P, Tsouderos Y, Delmas PD, Christiansen C. 2001 Incorporation and distribution of strontium in bone. *Bone* **28**, 446–453. (doi:10.1016/S8756-3282(01)00419-7)
6. Querido W, Farina M, Anselme K. 2015 Strontium ranelate improves the interaction of osteoblastic cells with titanium substrates: increase in cell proliferation, differentiation and matrix mineralization. *Biomatter* **5**, e1027847. (doi:10.1080/21592535.2015.1027847)
7. Li Y, Li X, Song G, Chen K, Yin G, Hu J. 2012 Effects of strontium ranelate on osseointegration of titanium implant in osteoporotic rats. *Clin. Oral Implants Res.* **23**, 1038–1044. (doi:10.1111/j.1600-0501.2011.02252.x)
8. Sips AJ, van der Vijgh WJ, Barto R, Netelenbos JC. 1995 Intestinal strontium absorption: from bioavailability to validation of a simple test representative for intestinal calcium absorption. *Clin. Chem.* **41**, 1446–1450.
9. Rizzoli R, Reginster JY. 2011 Adverse drug reactions to osteoporosis treatments. *Exp. Rev. Clin. Pharmacol.* **4**, 593–604. (doi:10.1586/ecp.11.42)
10. Andersen OZ *et al.* 2013 Accelerated bone ingrowth by local delivery of strontium from surface functionalized titanium implants. *Biomaterials* **34**, 5883–5890. (doi:10.1016/j.biomaterials.2013.04.031)
11. Schumacher M, Henss A, Rohnke M, Gelinsky M. 2013 A novel and easy-to-prepare strontium(II) modified calcium phosphate bone cement with enhanced mechanical properties. *Acta Biomater.* **9**, 7536–7544. (doi:10.1016/j.actbio.2013.03.014)
12. Thormann U *et al.* 2013 Bone formation induced by strontium modified calcium phosphate cement in critical-size metaphyseal fracture defects in ovariectomized rats. *Biomaterials* **34**, 8589–8598. (doi:10.1016/j.biomaterials.2013.07.036)
13. Schumacher M, Gelinsky M. 2015 Strontium modified calcium phosphate cements—approaches towards targeted stimulation of bone turnover. *J. Biomed. Mater. Res. B Appl. Biomater.* **3**, 4626–4640. (doi:10.1039/C5TB00654F)
14. Ginebra MP, Traykova T, Planell JA. 2006 Calcium phosphate cements: competitive drug carriers for the musculoskeletal system? *Biomaterials* **27**, 2171–2177. (doi:10.1016/j.biomaterials.2005.11.023)
15. Ginebra MP, Canal C, Espanol M, Pastorino D, Montufar EB. 2012 Calcium phosphate cements as drug delivery materials. *Adv. Drug Deliv. Rev.* **64**, 1090–1110. (doi:10.1016/j.addr.2012.01.008)
16. Schumacher M, Wagner AS, Kokesch-Himmelreich J, Bernhardt A, Rohnke M, Wenisch S, Gelinsky M. 2016 Strontium substitution in apatitic CaP cements effectively attenuates osteoclastic resorption but does not inhibit osteoclastogenesis. *Acta Biomater.* **37**, 184–194. (doi:10.1016/j.actbio.2016.04.016)
17. Alt V *et al.* 2013 A new metaphyseal bone defect model in osteoporotic rats to study biomaterials for the enhancement of bone healing in osteoporotic fractures. *Acta Biomater.* **9**, 7035–7042. (doi:10.1016/j.actbio.2013.02.002)
18. Kruppke B, Hose D, Schnettler R, Seckinger A, Rossler S, Hanke T, Heinemann S. 2018 Drug release as a function of bioactivity, incubation regime, liquid, and initial load: release of bortezomib from calcium phosphate-containing silica/collagen xerogels. *J. Biomed. Mater. Res. B Appl. Biomater.* **106**, 1165–1173. (doi:10.1002/jbm.b.33931)
19. Noukrati H, Cazalbou S, Demnati I, Rey C, Barroug A, Combes C. 2016 Injectability, microstructure and release properties of sodium fusidate-loaded apatitic cement as a local drug-delivery system. *Mater. Sci. Eng. C Mater. Biol. Appl.* **59**, 177–184. (doi:10.1016/j.msec.2015.09.070)
20. Aw MS, Khalid KA, Gulati K, Atkins GJ, Pivonka P, Findlay DM, Losic D. 2012 Characterization of drug-release kinetics in trabecular bone from titania nanotube implants. *Int. J. Nanomedicine* **7**, 4883–4892.
21. Giers MB, McLaren AC, Schmidt KJ, Caplan MR, McLemore R. 2014 Distribution of molecules locally delivered from bone cement. *J. Biomed. Mater. Res. B Appl. Biomater.* **102**, 806–814. (doi:10.1002/jbm.b.33062)
22. McLaren A, Giers MB, Fraser J, Hosack L, Caplan MR, McLemore R. 2014 Antimicrobial distribution from local delivery depends on dose: a pilot study with MRI. *Clin. Orthop. Relat. Res.* **472**, 3324–3329. (doi:10.1007/s11999-014-3493-1)
23. Caprioli RM. 2015 Imaging mass spectrometry: enabling a new age of discovery in biology and medicine through molecular microscopy. *J. Am. Soc. Mass Spectrom.* **26**, 850–852. (doi:10.1007/s13361-015-1108-z)
24. Fletcher JS, Vickerman JC. 2013 Secondary ion mass spectrometry: characterizing complex samples in two and three dimensions. *Anal. Chem.* **85**, 610–639. (doi:10.1021/ac303088m)
25. Rohnke M, Henss A, Kokesch-Himmelreich J, Schumacher M, Ray S, Alt V, Gelinsky M, Janek J. 2013 Mass spectrometric monitoring of Sr-enriched bone cements—from *in vitro* to *in vivo*. *Anal. Bioanal. Chem.* **405**, 8769–8780. (doi:10.1007/s00216-013-7329-8)
26. Henss A, Rohnke M, El Khassawna T, Govindarajan P, Schlewitz G, Heiss C, Janek J. 2013 Applicability of ToF-SIMS for monitoring compositional changes in bone in a long-term animal model. *J. R. Soc. Interface* **10**, 20130332. (doi:10.1098/rsif.2013.0332)
27. Schaepe K *et al.* 2018 Imaging of lipids in native human bone sections using ToF-SIMS, AP-SMALDI Orbitrap MS and Orbitrap-SIMS. *Anal. Chem.* **90**, 8856–8864. (doi:10.1021/acs.analchem.8b00892)
28. Rohnke M *et al.* 2017 Strontium release from Sr^{2+}-loaded bone cements and dissipation in healthy and osteoporotic rat bone. *J. Control Release* **262**, 159–169. (doi:10.1016/j.jconrel.2017.07.036)
29. Henss A *et al.* 2013 Quantification of calcium content in bone by using ToF-SIMS—a first approach. *Biointerphases* **8**, 31. (doi:10.1186/1559-4106-8-31)
30. Belu AM, Graham DJ, Castner DG. 2003 Time-of-flight secondary ion mass spectrometry: techniques and applications for the characterization of biomaterial surfaces. *Biomaterials* **24**, 3635–3653. (doi:10.1016/S0142-9612(03)00159-5)
31. Muddiman DC, Gusev AI, Hercules DM. 1995 Application of secondary ion and matrix-assisted laser desorption-ionization time-of-flight mass spectrometry for the quantitative analysis of biological molecules. *Mass Spectrom. Rev.* **14**, 383–429. (doi:10.1002/mas.1280140603)
32. Heiss C *et al.* 2012 Induction of osteoporosis with its influence on osteoporotic determinants and their interrelationships in rats by DEXA. *Med. Sci. Monit.* **18**, Br199–Br207. (doi:10.12659/MSM.882895)
33. Heinemann S, Rossler S, Lemm M, Ruhnow M, Nies B. 2013 Properties of injectable ready-to-use calcium phosphate cement based on water-immiscible liquid. *Acta Biomater.* **9**, 6199–6207. (doi:10.1016/j.actbio.2012.12.017)
34. Lode A, Heiss C, Knapp G, Thomas J, Nies B, Gelinsky M, Schumacher M. 2018 Strontium-modified premixed calcium phosphate cements for the therapy of osteoporotic bone defects. *Acta Biomater.* **65**, 475–485. (doi:10.1016/j.actbio.2017.10.036)
35. Bradt J-H, Mertig M, Teresiak A, Pompe W. 1999 Biomimetic mineralization of collagen by combined fibril assembly and calcium phosphate formation. *Chem. Mater.* **11**, 2694–2701. (doi:10.1021/cm991002p)
36. Bernhardt A, Lode A, Boxberger S, Pompe W, Gelinsky M. 2008 Mineralised collagen—an artificial, extracellular bone matrix—improves osteogenic differentiation of bone marrow stromal cells. *J. Mater. Sci. - Mater. Med.* **19**, 269–275. (doi:10.1007/s10856-006-0059-0)
37. Henss A, Hild A, Rohnke M, Wenisch S, Janek J. 2015 Time of flight secondary ion mass spectrometry of bone—impact of sample preparation and measurement conditions. *Biointerphases* **11**, 02A302. (doi:10.1116/1.4928211)
38. Boudaoud A, Burian A, Borowska-Wykret D, Uyttewaal M, Wrzalik R, Kwiatkowska D, Hamant O.

2014 FibrilTool, an ImageJ plug-in to quantify fibrillar structures in raw microscopy images. *Nat. Protoc.* **9**, 457–463. (doi:10.1038/nprot.2014.024)

39. Daghma DES, Malhan D, Simon P, Stotzel S, Kern S, Hassan F, Lips KS, Heiss C, El Khassawna T. 2018 Computational segmentation of collagen fibers in bone matrix indicates bone quality in ovariectomized rat spine. *J. Bone Miner. Metab.* **36**, 297–306. (doi:10.1007/s00774-017-0844-5)
40. Crank J. 1975 *The mathematics of diffusion*. Oxford, UK: Clarendon Press.
41. Schumacher M, Lode A, Helth A, Gelinsky M. 2013 A novel strontium(II)-modified calcium phosphate bone cement stimulates human-bone-marrow-derived mesenchymal stem cell proliferation and osteogenic differentiation *in vitro*. *Acta Biomater.* **9**, 9547–9557. (doi:10.1016/j.actbio.2013.07.027)
42. Schwarcz HP, Abueidda D, Jasiuk I. 2017 The ultrastructure of bone and its relevance to mechanical properties. *Front. Phys.* **5**, 39. (doi:10.3389/fphy.2017.00039)
43. Clarke B. 2008 Normal bone anatomy and physiology. *Clin. J. Am. Soc. Nephrol.* **3**(Suppl. 3), S131–S139. (doi:10.2215/CJN.04151206)
44. Osterhoff G, Morgan EF, Shefelbine SJ, Karim L, McNamara LM, Augat P. 2016 Bone mechanical properties and changes with osteoporosis. *Injury* **47**, S11–S20. (doi:10.1016/S0020-1383(16)47003-8)
45. Zebaze RM, Ghasem-Zadeh A, Bohte A, Iuliano-Burns S, Mirams M, Price RI, Mackie EJ, Seeman E. 2010 Intracortical remodelling and porosity in the distal radius and post-mortem femurs of women: a cross-sectional study. *Lancet* **375**, 1729–1736. (doi:10.1016/S0140-6736(10)60320-0)
46. Manolagas SC, Jilka RL. 1995 Bone marrow, cytokines, and bone remodeling. Emerging insights into the pathophysiology of osteoporosis. *N. Engl. J. Med.* **332**, 305–311. (doi:10.1056/NEJM199502023320506)
47. Teitelbaum SL. 2000 Bone resorption by osteoclasts. *Science* **289**, 1504–1508. (doi:10.1126/science.289.5484.1504)
48. McKee MD, Cole WG. 2012 Bone matrix and mineralization, pp. 9–37.
49. Reznikov N, Shahar R, Weiner S. 2014 Bone hierarchical structure in three dimensions. *Acta Biomater.* **10**, 3815–3826. (doi:10.1016/j.actbio.2014.05.024)
50. Li C, Paris O, Siegel S, Roschger P, Paschalis EP, Klaushofer K, Fratzl P. 2010 Strontium is incorporated into mineral crystals only in newly formed bone during strontium ranelate treatment. *J. Bone Miner. Res.* **25**, 968–975.
51. Specht AJ, Mostafaei F, Lin Y, Xu J, Nie LH. 2017 Measurements of strontium levels in human bone *in vivo* using portable X-ray fluorescence (XRF). *Appl. Spectrosc.* **71**, 1962–1968. (doi:10.1177/0003702817694383)
52. Boivin G, Farlay D, Khebbab MT, Jaurand X, Delmas PD, Meunier PJ. 2010 In osteoporotic women treated with strontium ranelate, strontium is located in bone formed during treatment with a maintained degree of mineralization. *Osteoporos. Int.* **21**, 667–677. (doi:10.1007/s00198-009-1005-z)